Evidence for hot clumpy accretion flow in the transitional millisecond pulsar PSR J1023+0038

T. Shahbaz,[1,2]★ Y. Dallilar,[3] A. Garner,[3] S. Eikenberry,[3] A. Veledina[4,5] and P. Gandhi[6]

[1]*Instituto de Astrofísica de Canarias (IAC), E-38200 La Laguna, Tenerife, Spain*
[2]*Departamento de Astrofísica, Universidad de La Laguna (ULL), E-38206 La Laguna, Tenerife, Spain*
[3]*Department of Astronomy, University of Florida, 211 Bryant Space Science Center, Gainesville, FL 32611, USA*
[4]*Nordita, KTH Royal Institute of Technology and Stockholm University, Roslagstullsbacken 23, SE-10691 Stockholm, Sweden*
[5]*Tuorla Observatory, University of Turku, Väisäläntie 20, FI-21500 Piikkiö, Finland*
[6]*Department of Physics and Astronomy, University of Southampton, Highfield, Southampton SO17 1BJ, UK*

ABSTRACT

We present simultaneous optical and near-infrared (IR) photometry of the millisecond pulsar PSR J1023+0038 during its low-mass X-ray binary phase. The r'- and K_s-band light curves show rectangular, flat-bottomed dips, similar to the X-ray mode-switching (active–passive state transitions) behaviour observed previously. The cross-correlation function (CCF) of the optical and near-IR data reveals a strong, broad negative anticorrelation at negative lags, a broad positive correlation at positive lags, with a strong, positive narrow correlation superimposed. The shape of the CCF resembles the CCF of black hole X-ray binaries but the time-scales are different. The features can be explained by reprocessing and a hot accretion flow close to the neutron star's magnetospheric radius. The optical emission is dominated by the reprocessed component, whereas the near-IR emission contains the emission from plasmoids in the hot accretion flow and a reprocessed component. The rapid active–passive state transition occurs when the hot accretion flow material is channelled on to the neutron star and is expelled from its magnetosphere. During the transition the optical reprocessing component decreases resulting in the removal of a blue spectral component. The accretion of clumpy material through the magnetic barrier of the neutron star produces the observed near-IR/optical CCF and variability. The dip at negative lags corresponds to the suppression of the near-IR synchrotron component in the hot flow, whereas the broad positive correlation at positive lags is driven by the increased synchrotron emission of the outflowing plasmoids. The narrow peak in the CCF is due to the delayed reprocessed component, enhanced by the increased X-ray emission.

Key words: binaries: close – stars: fundamental parameters – stars: individual: PSR J1023+0038 – stars: neutron – X-rays: binaries.

1 INTRODUCTION

Millisecond radio pulsars (MSPs) are believed to be the descendants of old, slowly rotating weakly magnetic field neutron stars that show radio, X-ray, and/or γ-ray pulsations that are present in low-mass X-ray binaries (LMXBs). The theory of recycled pulsars suggests that after the neutron star turns off its radio pulsations, the transfer of angular momentum from the low-mass companion star to the neutron star via accretion is responsible for the spin-up of the initially slowly rotating neutron star (Alpar et al. 1982;

Radhakrishnan & Srinivasan 1982). During this accretion phase, X-ray pulsations at the spin frequency of the neutron star are detected and the system shows the typical features of an accreting millisecond X-ray pulsar (AMXP). The recycling scenario of MSPs discussed above was initially confirmed by PSR J1023+0038 (Archibald et al. 2009), which was the first source that showed the transition between the rotation-powered state to the accretion-powered state. We now know of three transitional MSPs: PSR J1023+0038 (Archibald et al. 2009), XSS J12270−4859 (Bogdanov et al. 2014), and M28I (IGR J18245−2452; Papitto et al. 2013).

PSR J1023+0038 transitioned from a rotation-powered to an accretion-powered LMXB state in 2013 June (Stappers et al. 2013; Patruno et al. 2014; Takata et al. 2014) and so far has remained

★ E-mail: tsh@iac.es

in this state. The state transition involved the disappearance of the radio pulsed signal and an increase in the GeV flux by a factor of ~ 5 (Stappers et al. 2014). In the optical, the system brightened by ~ 1 mag and showed the presence of several broad emission lines typical of an accretion disc (Halpern et al. 2013). In the LMXB state, the X-ray luminosity varied between $\sim 10^{32.5}$ and $10^{34.5}$ erg s^{-1} showing three distinct states: (1) high 'active' state with $L_X \sim 3 \times 10^{33}$ erg s^{-1} present 80 per cent of the time; (2) low 'passive' state with $L_X \sim 5 \times 10^{32}$ erg s^{-1} present 20 per cent of the time; and (3) the 'flare' state with $L_X \sim 3 \times 10^{34}$ erg s^{-1} present for about 2 per cent of the time (Archibald et al. 2015; Bogdanov 2015). Coherent X-ray pulsations have been observed but appear only in the high state, and have been interpreted as being due to the inflowing accretion material heating the magnetic polar caps of rotating neutron star (Archibald et al. 2015). The transitions between the low and high states are very rapid with a time-scale of 10 s and results in rectangular-shaped dips in the X-ray light that seem to be ubiquitous in all of the X-ray observations. Similar variability has also been observed at optical wavelengths with rectangular dip ingress and egress times of ~ 20 s (Bogdanov & Halpern 2015; Shahbaz et al. 2015). However, given the limited simultaneous optical/X-ray observations, it is not clear if the X-ray and optical dips are direct counterparts of each other. Simultaneous *XMM–Newton* X-ray and *B*-band optical light curves show X-ray dips that do not usually have corresponding optical dips (Bogdanov 2015). However, the uncertainties in the *B*-band data are large and given that the dips in the blue are weak (Shahbaz et al. 2015), one cannot rule out if the dips are present.

In this paper we present the results of simultaneous optical/near-infrared (IR) fast imaging of PSR J1023+0038. We determine the autocorrelation function (ACF) of the optical and near-IR light curves and the cross-correlation (CCF) function of the two light curves. We explain the observed features of the ACFs and CCFs as due to the hot, clumpy inner accretion flow close to the pulsar's magnetosphere.

2 OBSERVATIONS AND DATA REDUCTION

2.1 High-speed optical photometry

Fast optical imaging of PSR J1023+0038 was carried out on the night of 2017 February 8 using Auxiliary-port CAMera (ACAM) on the 4.2 m William Herschel Telescope (WHT). The CCD was binned by a factor of 2 and windowed down to 200×400 pixels, which reduced the dead time between exposures to only 1.85 s. The plate scale was 0.25 arcsec pixel^{-1}. We used the *r'* filter and an exposure time of 2.0 s that resulted in a time resolution of 3.85 s. Observations were obtained from 2017 February 9 01:37:21 to 05:31:29 UT and the seeing was typically between 1.0 and 2.0 arcsec.

The images were first bias-subtracted and flat-fielded. The target counts were then extracted using optimal photometry with a seeing-dependent variable circular aperture tracking the centroid of the source on each image. The sky background was measured from the clipped mean in an annular aperture around the target. Relative photometry of PSR J1023+0038 was then carried out with respect to the local standard star SDSS J102343.30+003819.1 *r'* = 14.778. The mean magnitude of PSR J1023+0038 was *r'* = 16.48.

2.2 High-speed near-infrared photometry

Fast near-IR imaging of PSR J1023+0038 was carried out on the night of 2017 February 8 using Canarias InfraRed Camera Experiment (CIRCE; Eikenberry et al. 2017) on the 10.4 m Gran Telescopio Canarias (GTC). The plate scale of the array was 0.1 arcsec pixel^{-1} and the image size was 1855×1365 pixels. The K_s filter was used with an exposure time of 5.0 s and a dead time of 1 s, resulting in a time resolution of 5 s. A five-point dither pattern was used with five exposures at each dither position. Observations were obtained from 2017 February 9 01:12:21 to 05:31:04 UT. Dark images were also taken with the same detector configuration and exposure time.

The CIRCE data reduction was carried out using the SuperFATBOY[1] data reduction pipeline. We first performed the linearity correction and dark subtraction on all the images. A flat-field was then generated and applied to the science images. The sky background was determined using the images in each dither pattern. Finally, bad pixels and cosmic ray events were interpolated and the images binned by 2 pixels to improve signal-to-noise ratio.

Before extracting the counts from the stars in the field the images were first shifted and aligned. We used optimal photometry with a seeing-dependent variable circular aperture tracking the centroid of the source on each image to determine the star counts. The sky background was measured from the clipped mean in an annular aperture around the target. Relative photometry of PSR J1023+0038 was then carried out with respect to the local standard star 2MASSX J10235051+0038163 with $K_s = 14.894$ (the ACAM local standard could not be used because it occasionally fell into the cosmetic gap of the IR array). The mean magnitude of PSR J1023+0038 was $K_s = 15.14$.
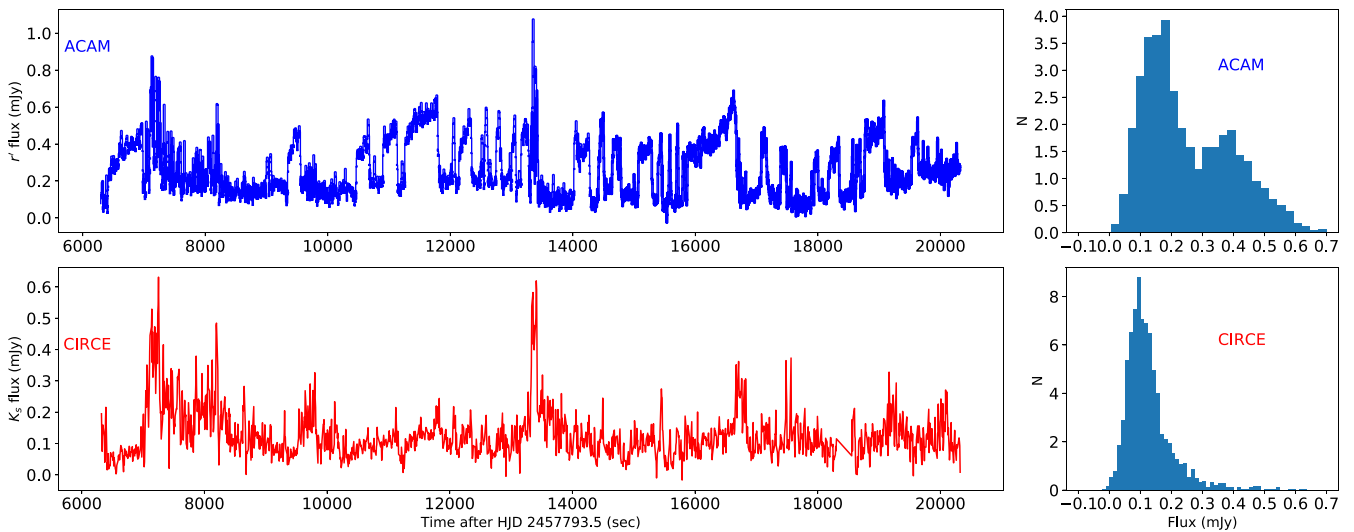
3 LIGHT CURVES

Fig. 1 shows the observed flux *r'*- and K_s-band light curves of PSR J1023+0038 and a comparison star of similar brightness, where we converted the magnitudes to flux density using the appropriate zero-point for each band. The *r'*-band light curve clearly show the secondary star's heated ellipsoidal modulation with superimposed flaring activity. Flares and rectangular-shaped dips are present similar to previous optical light curves (Bogdanov 2015; Shahbaz et al. 2015). We also show the light curves of the comparison stars. As one can see there is some low-level structure in the K_s-band comparison star light curve.

Fig. 2 shows the dereddened, detrended *r'*- and K_s-band flux light curves. We used a colour excess of $E(B - V) = 0.073$ (Shahbaz et al. 2015) and $A_V/E(B - V) = 3.1$ (Cardelli, Clayton & Mathis 1989) to dereddened the magnitudes and then converted the magnitudes to flux density. Finally we detrended the light curves using a third- and first-order polynomial for the *r'*- and K_s-band light curves, respectively. The passive, active, and flare states are clearly seen in the *r'*-band light curve rectangular, flat-bottomed dip features are apparent, which are similar to the mode-switching behaviour (passive and active states) that has been observed in the X-ray and optical light curves (Tendulkar et al. 2014; Bogdanov 2015; Shahbaz et al. 2015). The histogram of the dereddened, detrended *r'*-band flux values (see Fig. 2) clearly shows a bimodal distribution between the passive and active states. Such a distribution is not so apparent in the K_s-band light curve. This is because the rectangular dips in the *r'*-band light curve are deeper than the dips in the K_s-band light curve; the active minus passive (active − passive) flux

---

[1] SuperFATBOY is an XML-controlled GPU-enabled PYTHON pipeline developed at the University of Florida.
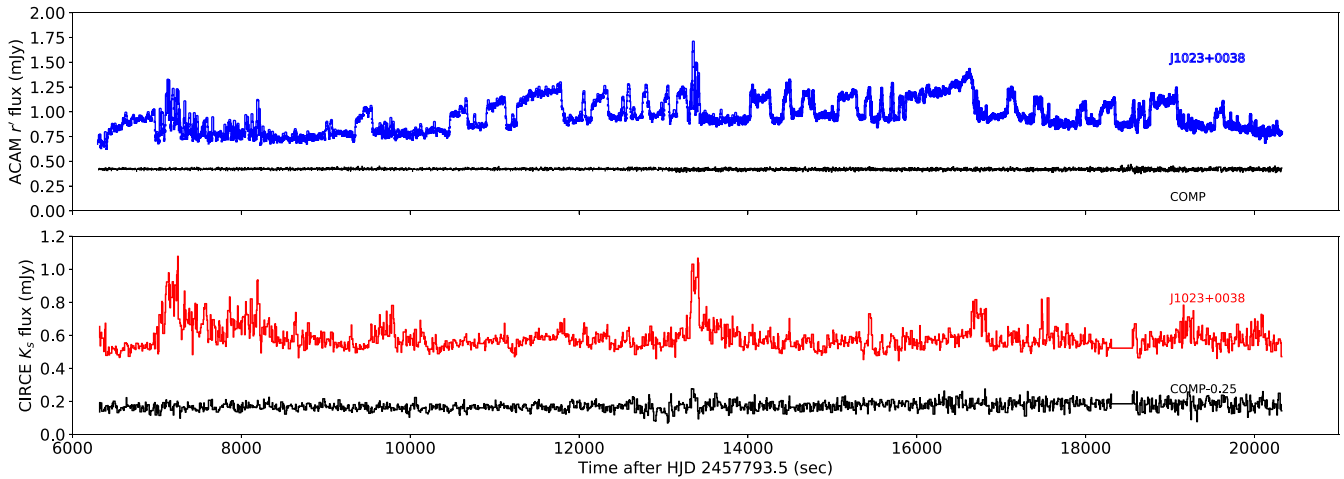
Figure 1. Observed light curves of PSR J1023+0038 and comparison star taken with the WHT+ACAM (r' band) and GTC+CIRCE (K_s band). The light curve of the (K_s band) comparison star has been shifted by 0.5 for clarity.

Figure 2. The dereddened and detrended r'- and K_s-band light curves of PSR J1023+0038. The right-hand panel in each plot shows the histogram of the flux values. The active- and passive-state bimodal behaviour is clearly evident in the r'-band light curve.

of the dereddened light curves is 0.40 and 0.14 mJy for the r'- and K_s-band light curves, respectively.

3.1 Light-curve correlations

In an attempt to understand the origin and emission mechanism of the optical and near-IR light curves, we calculate the ACF of the optical and near-IR light curves and the CCF between the observed optical and near-IR light curves. The analysis is a simple determination of the relative time variability between the two wavelength-dependent light curves and provides a clear, uncomplicated (average) comparison of the two signals with respect to time. The ACF represents a correlation of a light curve with itself, and gives a measure of the effective coherence time-scales in the data. The CCF represents the convolution of two light curves and reveals whether they have the same features and the time delay between them. To determine the ACF and CCF between two light curves (i.e. the cross-correlation coefficient versus time delay between the light curves) we compute the discrete correlation function (DCF) using

PYDC,[2] which works well with unevenly sampled data (Edelson & Krolik 1988; Robertson et al. 2015). Positive time lags mean that the optical leads the near-IR, whereas negative time lags mean that the optical lags the near-IR. To calculate the ACF we use the whole light curve and the time resolution of the data. To calculate the CCF between optical and near-IR light curves we only use data that are simultaneous (14 000 s). Given that time resolution of the r'-band data is better than the K_s-band data, when calculating the CCF we rebin the light curves to the best time resolution of the K_s-band data.

3.1.1 ACFs

In Fig. 3 we show the ACF of entire r'- and K_s-band light curves of PSR J1023+0038. The r'- and K_s-band ACFs have different widths; with a full width at half-maximum (FWHM) of 130 and 90 s, respectively. Above ∼70 s, the K_s-band ACF is broader than the r'-band

[2] https://github.com/astronomerdamo/pydcf
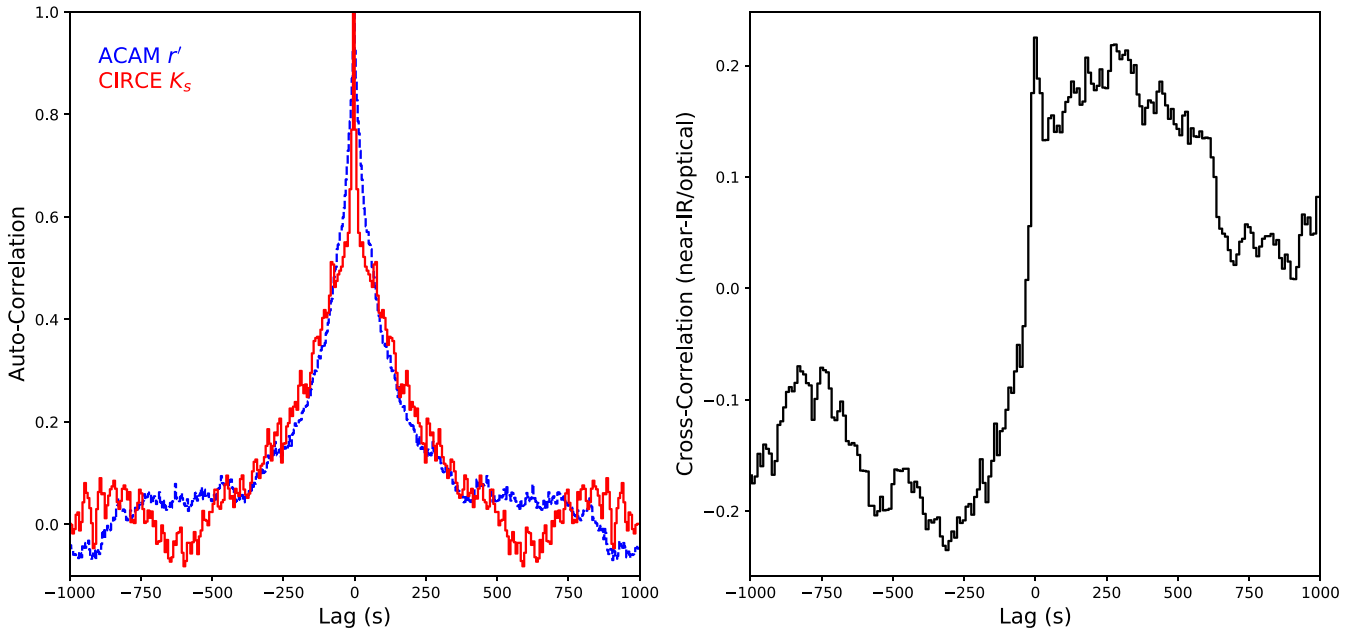
Figure 3. Left: ACF of the CIRCE K_s (red solid line) and ACAM r' (blue dashed line) PSR J1023+0038 light curves as a function of time delay. The near-IR is broader than the optical ACF. Right: CCF between the simultaneous K_s and r' light curves as a function of time delay. A strong anticorrelation is observed where near-IR light curve is delayed with respect to optical light curve by ∼300 s.
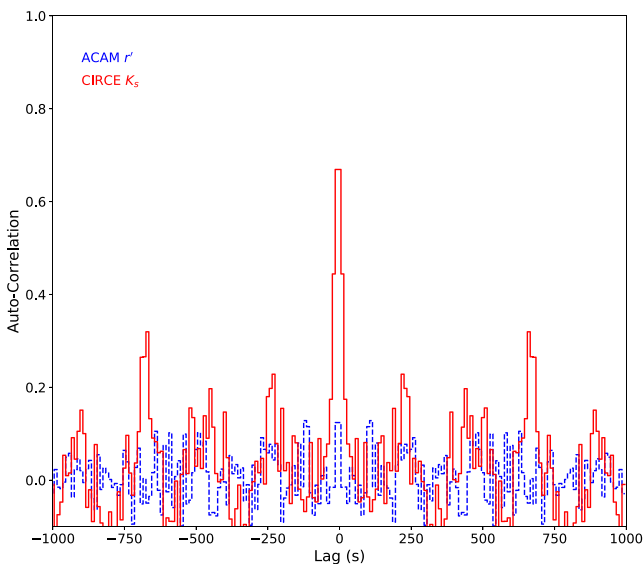
Figure 4. The ACF of the CIRCE K_s (red solid line) and ACAM r' (blue dashed line) comparison star light curves. The near-IR ACF has a width of ∼40 s.

ACF, which argues for a reprocessing origin for the slowly variable component, most likely in the outer regions of the accretion disc. However, very close to the core, the r'-band ACF is broader than the K_s-band ACF, which argues against a simple reprocessing origin (see Section 4.3). The K_s-band comparison star light curve (see Fig. 1) shows some low-level correlated variability. Indeed, this is seen in its ACF (see Fig. 4), which has a non-zero width, with a FWHM of 40 s, similar to the time-scale of the dither pattern (see Section 2.2). In contrast, the ACF of the r'-band comparison star light curve does not show any peaks. This suggests that there are some low-level systematics in the data reduction of the near-IR data possibly due to undercorrected cosmetic defects in the CIRCE

engineering-grade detector array. Hence, the true width of the ACF of PSR J1023+0038 is smaller.

In Fig. 3 we show the optical and near-IR CCF using all the simultaneous optical and near-IR data (14 000 s). The negative lag implies the optical band is delayed with respect to the near-IR, whereas an anticorrelation implies that the variability between the near-IR and optical fluxes is out of phase. We observe a strong, broad negative anticorrelation on time-scales of ∼−300 s, a broad positive correlation near-IR lag at ∼+300 s, and a strong, positive, and narrow correlation at ∼+5 s (see Fig. 3).

To see if there is a time-dependent evolution in the ACF and CCF we compute the dynamic ACF and CCFs (see Fig. 5) calculated using a windows size of 1000 s and a step size of 500 s, i.e. overlapping sections where every second ACF/CCF is independent. A mean CCF is then derived for each time series pair, which effectively acts as a high-pass filter, and variations with time-scales longer than ∼500 s do not appear. One can see, the K_s-band ACF is not always broader than the r'-band ACF, the width of the ACFs changes with time.

3.1.2 Light curves

In Fig. 6 we show the detrended light curves and the r'/K_s flux ratio and the r'/K_s versus K_s-band flux ratio diagram, for each 2000 s block of data. The yellow and green points mark the passive and active states, respectively, which are also shown in the r'/K_s light-curve plot. During the transition from the active to passive state, the r'/K_s flux ratio decreases because there is a larger decrease in the r'-band flux compared to the K_s-band flux: there is a removal of a blue spectral component.

3.2 Power density spectrum

In Fig. 7 we show power density spectrum (PDS) of the dereddened optical and near-IR light curves of PSR J1023+0038 (see Section 3). We use the Lomb–Scargle method to compute the periodograms
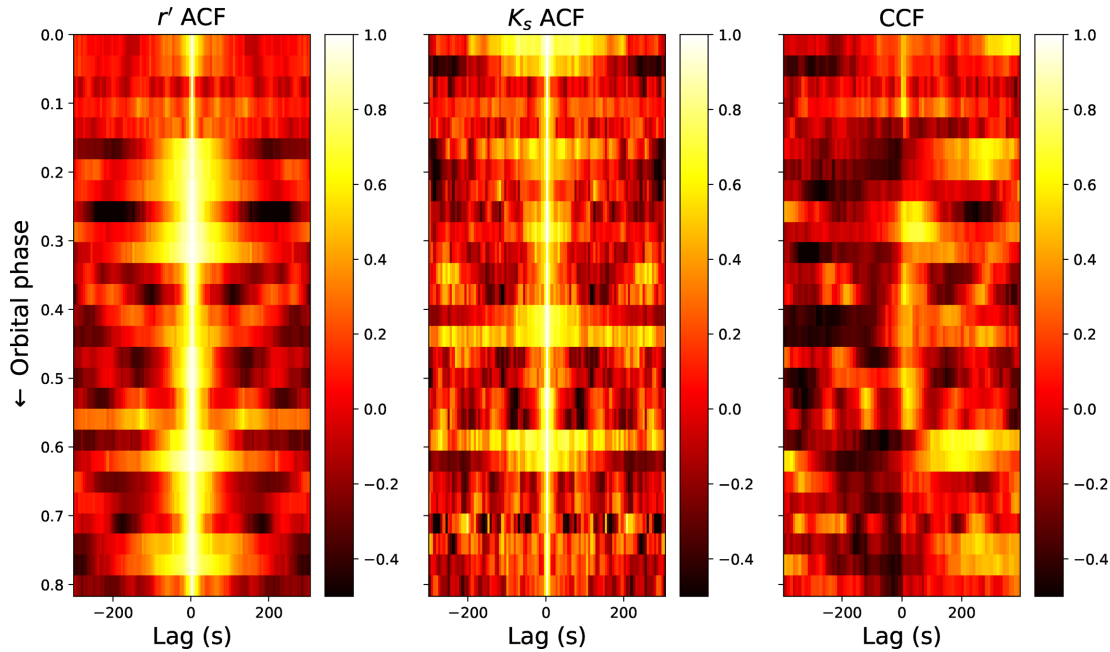
Figure 5. The dynamical ACF of the *r'* (left) and K_s-band (middle) light curves and the CCFs (right) of the two light curves. We use a windows size of 1000 s and a step size of 500 s. Each horizontal line is a single ACF or CCF from a 500 s segment light curve. The orbital phase ephemeris is taken from Shahbaz et al. (2015).

(Press et al. 1992) with the constraints imposed by the Nyquist frequency, the typical duration of each observation and use the recipe given in Horne & Baliunas (1986) to calculate the number of independent frequencies. We then bin and fit the PDS in logarithmic space (Papadakis & Lawrence 1993), where white noise level was subtracted by fitting the highest frequencies with a white noise (constant) plus red noise (power law; $P \propto \nu^\beta$) model (only for the PSR J1023+0038 light curves). We find that the PDS of the *r'*- and K_s-band light curve of PSR J1023+0038 is dominated by a red noise component with a power-law index of $\beta = -1.34 \pm 0.04$ and -1.04 ± 0.08, respectively, typical of aperiodic activity in X-ray binaries and X-ray transients in outburst and quiescence, which have β in the range -1.0 to -2.0 (Hynes et al. 2003; Shahbaz et al. 2003, 2004, 2005, 2010, 2013; Zurita, Casares & Shahbaz 2003). The power-law index of the *r'*- and K_s-band comparison star PDS is $\beta = 0.04 \pm 0.04$ and -0.22 ± 0.04, respectively. The *r'*-band PDS is consistent with zero, however, for the K_s band, the power-law index is significant, suggesting that there are systematic effects in the data (the PDS of the light curves using of a different local standard is also non-zero), possibly due to undercorrected cosmetic defects in the CIRCE engineering-grade detector array.

When determining the light curve of PSR J1023+0038 we divided the counts of PSR J1023+0038 into the counts of the local standard that does not vary To investigative the effects of using a red-noise-dominated local standard star (which has some low level variability) when computing the differential light curve of PSR J1023+0038 and comparison star, we perform a Monte Carlo simulation where we generate light curves with exactly the same sampling and integration times as the PSR J1023+0038 data. For each Monte Carlo, we simulate two light curve (LC_1 and LC_2) using the method of Timmer & Koenig (1995), with different PDS power-law indices β_1 and β_2, respectively. We divide the two light curves ($LC = LC_2/LC_1$) and calculate the PDS. We perform 1000 simulations, bin and fit the PDS in logarithmic space (Papadakis & Lawrence 1993), and then determine the PDS power-law index β.

We assume that the local standard (LC_1) has low-level variability with $\beta_1 = 0.0$–0.50, whereas the target of interest (LC_2) is dominated by red noise, where $\beta_2 = 0.5$–1.5. Our simulations show that β lies between β_1 and β_2, i.e. the red-noise-dominated local standard light curve (LC_1) makes power-law index of the differential light curve (LC) less steep. Fig. 8 shows the results of a simulation where final light curve LC has $\beta = -1.04$. As one can see the real PDS power-law index (β_2) of the target light curve LC_2 is steeper than the power-law index of differential light curve LC, $\beta_2 < \beta$. Although we cannot determine the real power-law index of the PDS of the K_s-band light curve because we do know the PDS power-law index of the local standard star used in the near-IR PSR J1023+0038 analysis. All we can say is that the near-IR light curve of PSR J1023+0038 has a PDS of $< -1.04 \pm 0.08$. Given that the PDS of the comparison star is -0.22 ± 0.04, at most we expect a similar amount of variability in the local standard star. Hence, we find that *r'*-band PDS is steeper than the K_s-band PDS. Both PDS have similar power at low frequencies, however, the K_s-band PDS has more variability at high frequencies.

4 DISCUSSION

4.1 The spectral energy distribution of the rectangular dips

To date there are three (PSR J1023+0038, M28I and XSS J12270−4859) transitional pulsars systems that transition between accretion-powered LMXB and rotation-powered radio pulsar states (Archibald et al. 2009; Papitto et al. 2013; Bassa et al. 2014). Of these systems PSR J1023+0038 and XSS J12270−4859 show rapid (<10 s) transitions from a high X-ray luminosity active state to a low luminosity passive state. In PSR J1023+0038 similar optical transitions are observed but on a slightly longer time-scale (~ 20 s). Simultaneous *XMM–Newton* X-ray and *B*-band optical light curves show X-ray dips that do not usually have corresponding optical dips (Bogdanov 2015). However, given that the *B*-band dips are much
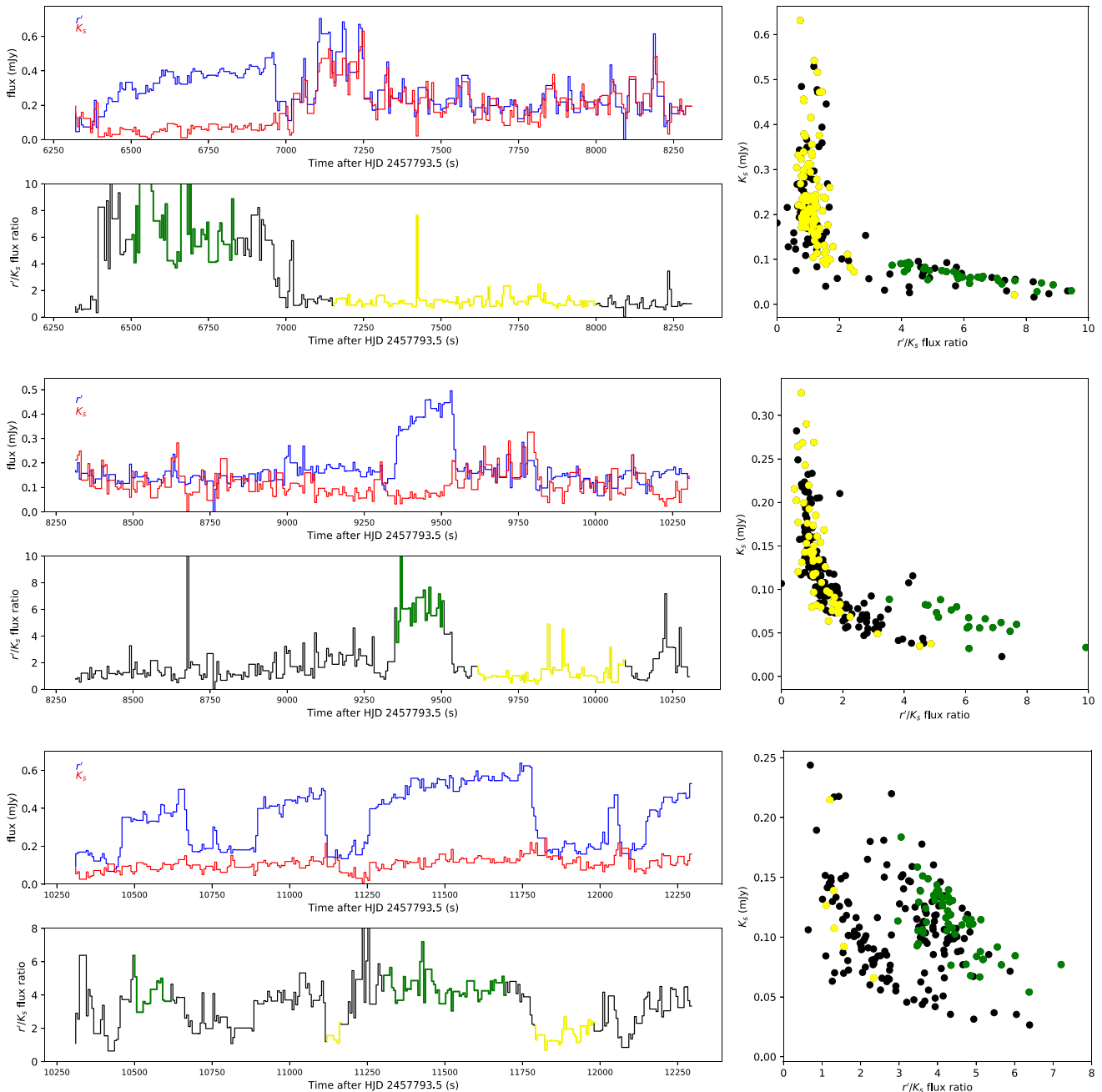
Figure 6. The light curves of PSR J1023+0038 split into seven 2000 s sections. Top left: the dereddened and detrended r'- and K_s-band light curves. Bottom left: the r'/K_s flux ratio light curve. Right: the r'/K_s versus K_s flux ratio diagram. The yellow and green points mark examples of passive and active state, respectively, which are shown in the r'/K_s light-curve plot (bottom right).

weaker compared to in the r' band (Shahbaz et al. 2015) combined with the large uncertainties in the B-band data, one cannot rule out if the dips are present and one cannot rule out that the X-ray and optical dips are direct counterparts of each other.

Shahbaz et al. (2015) therefore suggest that the optical analogue of the X-ray model switching may be due to reprocessing of the X-ray signal.

During the active state X-ray pulsations are observed, which implies that matter is being channelled on to the neutron star's magnetic poles. However, during the passive state there is no sign of X-ray pulsations (de Martino et al. 2013; Bogdanov et al. 2014;

Archibald et al. 2015; Papitto et al. 2015). Indeed, optical pulsations have also been observed that are interpreted as being due to synchrotron emission by relativistic electrons and positrons in the pulsar magnetosphere (Ambrosino et al. 2017). In the proposed model, the particles residing at a constant fraction of the light cylinder radius have a power-law energy distribution and emit incoherent synchrotron radiation (Pacini & Salvati 1983). The synchrotron self-absorption produces a turnover in the spectral energy distribution (SED). Indeed, in the Crab there is evidence for synchrotron self-absorption that is observed as a turnover in the SED near the H band (O'Connor, Golden & Shearer 2005).
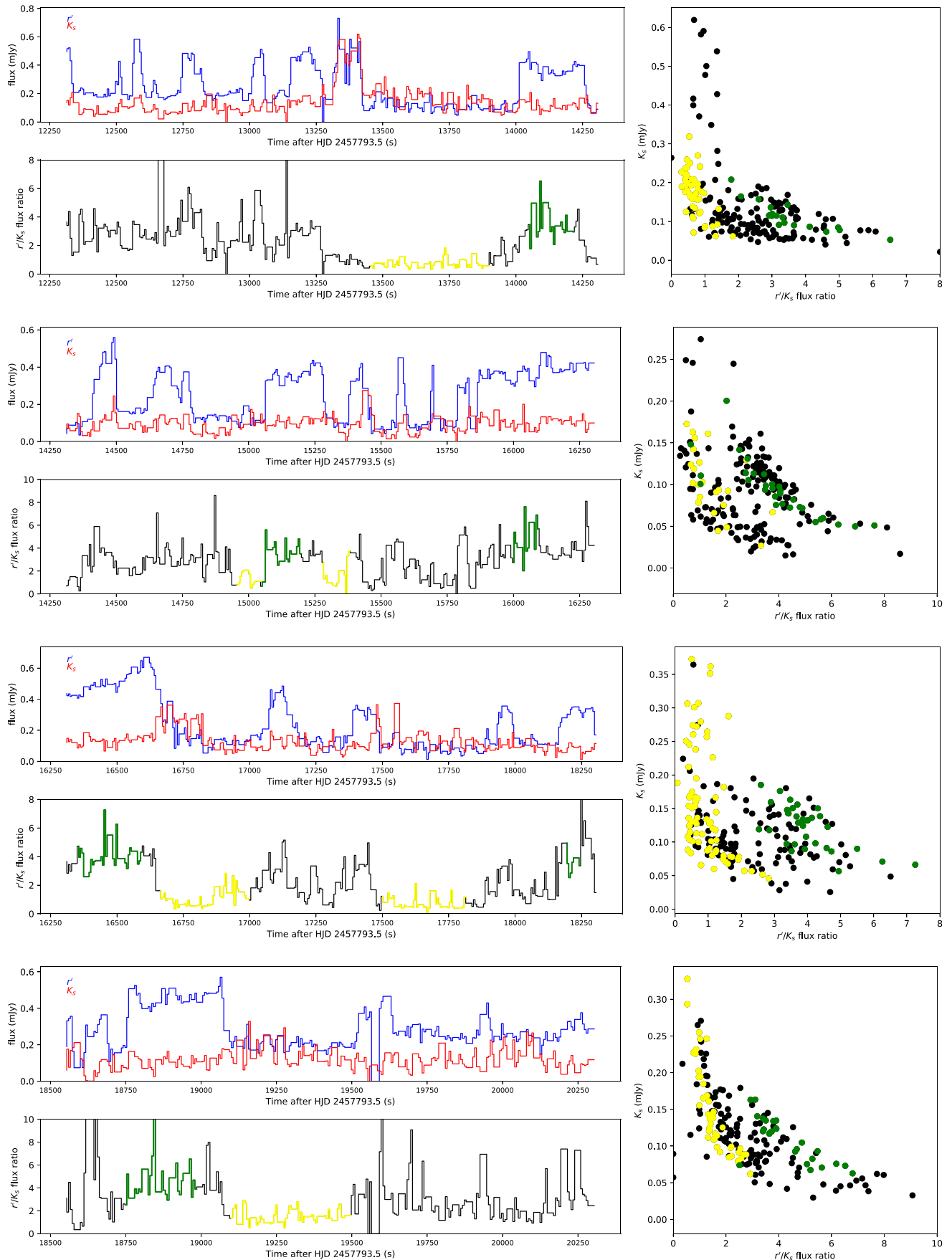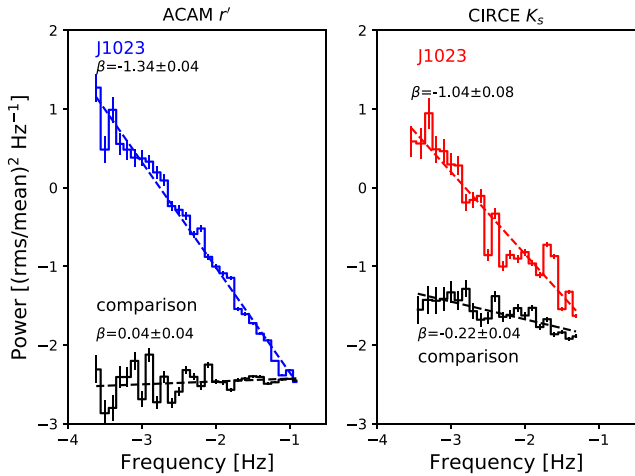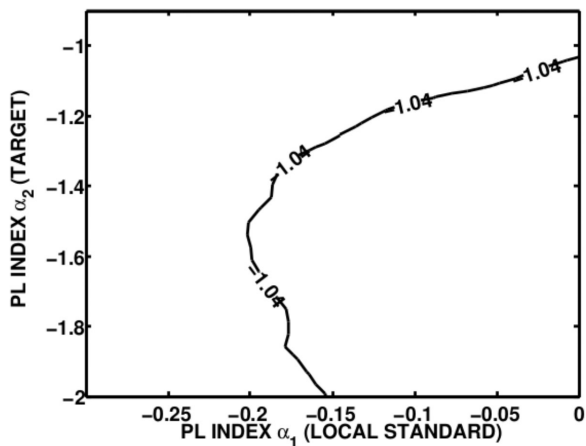
Figure 6 – *continued*

Figure 7. The PDS of the r'- (left) and K_s-band (right) light curves of PSR J1023+0038 and the comparison star. In each plot the dot–dashed lines show a power-law fit to the PDS.

Figure 8. The effects of red noise on the differential light curve of a target and local standard light curve. The light curves are calculated using the method of Timmer & Koenig (1995), with different PDS power-law indices β_1 and β_2 for the target and local standard light curve, respectively. The resulting differential light curve has a PDS power-law index of β. The plot shows a contour where $\beta = -1.04$. The true PDS power-law index (β_2) of the target light curve is steeper than the power-law index of differential light curve β.

Simultaneous X-ray and radio observations have revealed key features (Bogdanov et al. 2018). First, an anticorrelation between the X-ray and radio flux in the active and passive states. During the X-ray active state, the radio luminosity is low and X-ray pulsations are observed, but when the source transitions into the passive state, the pulsations disappear and the radio emission increases rapidly. Secondly, during the X-ray passive state, the radio spectrum evolves from a self-absorbed to optically thin spectrum on time-scales of several minutes, reminiscent of a classical evolving synchrotron spectrum. Bogdanov et al. (2018) conclude the radio flares are due to expanding synchrotron emitting plasma arising from the inner regions of the accretion disc.

In Fig. 9 we show the SED of the u'-, g'-, and r'-band dips observed in 2015 by Shahbaz et al. (2015) and the r'- and K_s-band dips observed in 2017 (see Section 3). The SED shows a turnover that is what one expects if the synchrotron emission arises
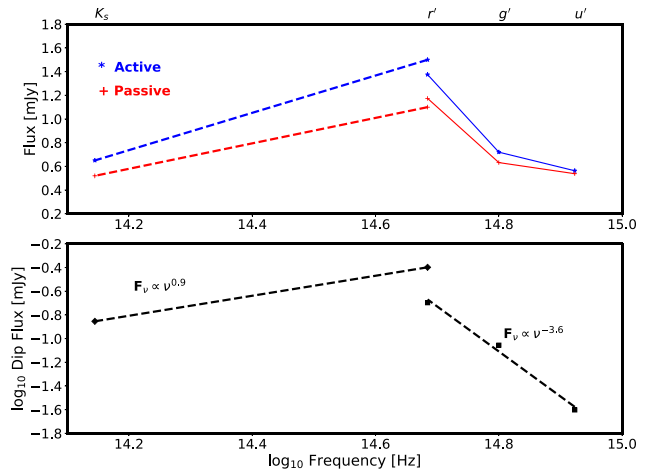
Figure 9. Top: the SED of the active (blue stars) and passive (red crosses) state. The $u'g'r'$-band data (solid line) were taken in 2015 and are presented in Shahbaz et al. (2015) and the r', K_s points (dashed line) were taken in 2017 presented in Section 3. Bottom: the active minus passive (active − passive) flux SED. The filled squares and filled diamonds show the data taken in 2015 and 2017, respectively. The dashed line shows a power-law fit of the form $F_\nu \propto \nu^\alpha$. A turnover in the SED lies somewhere between the r'- and K_s band. The active and passive fluxes are dereddened and contain flux from the secondary star, accretion disc, and synchrotron emission of plasmoids and reprocessing (see Section 4.4).

from an expanding synchrotron emitting plasma (Bogdanov et al. 2018) or synchrotron emission by relativistic electrons and positrons (Ambrosino et al. 2017). The synchrotron emission idea is also supported by the high K_s-band PDS variability at high frequencies (inner disc regions; see Section 3.2), which is what one expects for emission is non-thermal, likely from optically thin synchrotron emission.

An alternative explanation for the turnover in the SED of the dips is from a combination of clumpy accretion and irradiation. In Fig. 6 we show the r'/K_s versus K_s-band flux ratio diagram for different sections of the data. As one can see, during the transition from the active to passive state, the r'/K_s flux ratio decreases because there is a larger decrease in the r'-band flux compared to the K_s-band flux, i.e. there is a disappearance of a blue component. This is what one would expect if the reprocessing optical component is removed during the active–passive state transitions while the synchrotron component remains constant (see Section 4.4). In contrast Shahbaz et al. (2015) observed the disappearance of a red spectral component and attributed it to the removal of an irradiated disc. The difference between the r'-band dip observed in 2015 and 2017 (see Fig. 9) is due to the different amounts of clumpy material at the time of the observations. The combination of the removal of a red and blue component with different strengths gives rise to a turnover in the SED that lies somewhere between the r'- and K_s band.

4.2 Comparison with X-ray binaries

Simultaneous optical and X-ray observations of X-ray binaries have revealed multicomponent optical variability on subsecond time-scales, arising from components such as a hot inner flow, accretion disc reprocessing, and a jet. These appears to be a common feature in many X-ray binaries during the hard state and results in as narrow positive peak is the observed in the CCF, superimposed on an anticorrelation (Kanbach et al. 2001; Malzac et al. 2003; Durant et al. 2008, 2011; Gandhi et al. 2008). Intense and rapid

subsecond flaring is also seen and in a few systems it has been attributed to synchrotron emission from a jet (Hynes et al. 2003; Malzac, Merloni & Fabian 2004; Gandhi et al. 2010). On time-scales of minutes Swift J1753.5−0127 has shown strong optical variations (Durant et al. 2009). Veledina et al. (2015, 2017) have shown that the X-ray and optical variability in Swift J1753.5−0127 (Durant et al. 2008) is well reproduced by a simple model assuming that the optical variability is a mixture of X-ray reprocessing plus a hot flow synchrotron component that is exactly anticorrelated with respect to the X-rays. The hot flow model has also been used to explain the anticorrelated optical/X-ray behaviour in BW Cir (Pahari et al. 2017). Near-IR variations on time-scales of minutes have been observed in GRS 1915+105 and have been associated with synchrotron-emitting plasma (Fender et al. 1997; Eikenberry et al. 1998).

The shape of the optical/near-IR CCF of PSR J1023+0038, with the anticorrelation and a sharp rise at zero lag, resembles the optical/X-ray CCFs found in X-ray binaries, indicating an interplay of, at least, two separate components. This scenario was originally proposed for black hole X-ray binaries (Veledina, Poutanen & Vurm 2011), where the correlated component comes from the reprocessing of the incident X-ray flux, and the anticorrelated component originates from the hot accretion flow emitting in the optical via synchrotron. The time-scale of the optical and near-IR variability and correlations we observe in PSR J1023+0038 are, however, much longer than what is observed in other X-ray binaries.

A hot accretion flow can, in principle, exist close to the pulsar magnetosphere and can be occasionally expelled away by the rotating magnetic field (Parfrey, Spitkovsky & Beloborodov 2017). Such synchrotron-emitting outflowing plasmoids arising from the inner regions of the accretion disc could then be responsible for the increased radio emission during the X-ray passive states (Bogdanov et al. 2018). Given the low luminosity, and hence, low accretion rate and electron number density in PSR J1023+0038 the hot flow synchrotron emission is likely to be optically thin down to the near-IR. The entire spectrum is thus similar to those of the outer parts of the hot flow for higher accretion rates (Veledina, Poutanen & Vurm 2013; Poutanen, Veledina & Revnivtsev 2014). A combination of the red synchrotron spectrum with the blue spectrum of reprocessed radiation (Veledina et al., in preparation) can produce the observed power law $F_\nu \propto \nu^{0.9}$ (see Fig. 9).

The shape of the optical/near-IR CCF of PSR J1023+0038 somewhat resembles the optical/X-ray CCF observed in the black hole X-ray binary Swift J1753.5−0127 (Durant et al. 2008). However, the characteristic time-scales are different by an order of magnitude, and the broad positive peak at positive lags is missing in the CCF of Swift J1753.5−0127. The difference can be explained by the presence of a solid surface and neutron star magnetosphere in PSR J1023+0038. Because the accretion disc is truncated at this radius, the characteristic viscous time-scales are somewhat longer than in black hole binaries, giving broader features in the CCF. The absence of the broad peak at positive lags can be due to disappearance of the plasmoids under the event horizon, rather than their ejection, as is the case of PSR J1023+0038.

4.3 Light-curve correlations

Reprocessing of high-energy photons to lower energies in an extended accretion disc is thought to dominate the observed optical and near-IR fluxes. The expected cross-correlation signature is delayed because of the light travel time and smeared response of the optical and near-IR light curves with respect to the X-ray light curve. The optical and near-IR light curves are the convolution of the X-ray light curve with a broad transfer function representing the response of the extended accretion disc. The inner regions of the accretion disc reprocess high-energy X-rays into the soft X-rays/ultraviolet (UV) bands. Therefore, we expect the near-IR ACF to be broader than the optical CCF and the CCF to show a single strong, positive peak at positive lags (near-IR arriving after optical).

At first sight the ACFs of the entire r'- and K_s-band light curves have different width cores and wings (see Section 3.1.1). Above ∼70 s, the K_s-band ACF is broader than the r'-band ACF, which argues for a reprocessing origin for the slowly variable component, most likely in the outer regions of the accretion disc. However, very close to the core, the r'-band ACF is broader than the K_s-band ACF, which argues against a simple reprocessing origin. A detailed look at the ACF for different segments in time reveals that on average the r'-band ACF is a factor of ∼3–4 times broader than the K_s-band ACF (see Fig. 5), which is not what one would expect from a reprocessing model. A broader K_s-band ACF is expected if the K_s-band PDS is steeper than the r'-band PDS (Peterson 2001), which implies that there is more aperiodic variability from the accretion disc at low frequencies (outer disc regions) in the K_s-band light curve compared to the r'-band. However, we find that the r'-band PDS is steeper than the K_s-band PDS (even allowing for the systematic effects, see Section 3.1.1) and that the K_s-band PDS has more variability at high frequencies from the inner regions of the accretion disc/pulsar magnetosphere (see Section 3.2). This is what one expects for emission from a non-thermal component such as optically thin synchrotron emission.

The CCF of the simultaneous optical and near-IR data reveals a strong, broad negative anticorrelation and negative lags and a broad positive correlation at positive lags, with a strong, positive and narrow correlation superimposed (see Fig. 3). The broad positive correlation implies that the optical leads the near-IR flux. However, the broad negative delay implies the optical band is delayed with respect to the near-IR, and the anticorrelation implies that the variability between the near-IR and optical fluxes is out of phase.

The narrow correlation implies that optical leads the near-IR flux, consistent with a reprocessing origin. The ∼+5 s correlation is similar to the time-scale we would expect for the light travel time between the binary components. The light travel times of photons arise from the differences between the time of flight of photons that are observed directly and those that are reprocessed and reemitted before travelling back to the observer. For PSR J1023+0038 with an orbital period of 4.75 h, the corresponding binary separation of ∼1.8 $R_\odot$ (assuming a total binary mass of 2 $M_\odot$) implies a light travel time of ∼4 light-seconds. However, given that the delay is not phase resolved, it is not always present in the CCFs (see Fig. 6), suggesting that it is not due to the reprocessing on the secondary star, but is due to reprocessing in the accretion disc.

4.4 The hot accretion flow model

The observed broad anticorrelation at negative lags implies that the optical flux is delayed with respect to the near-IR flux, and the anticorrelation implies that the variability between the near-IR and optical fluxes is out of phase. These features are not due to reprocessing because a reprocessing CCF would rise quickly near zero and fall less quickly towards positive lags (O'Brien et al. 2002). The broad components of the CCF and the sudden change near zero lag are strong indicative of at least two separate processes superposed in

the light curves, such as a hot flow for the anticorrelation and a reprocessing/jet component for the positively correlated optical/near-IR components. A combination of reprocessing and the interaction of a hot flow with the pulsar magnetosphere can produce the observed optical/near-IR correlations.

Given that the reprocessed emission is expected to have a blue spectrum, we expect it to be more prominent in the r' band compared to in the K_s band. We propose that the r'-band emission is totally dominated by the reprocessed component, while the K_s band contains both synchrotron and reprocessed emission. In the optical, the reprocessing component dominates the active state transition and decreases during the transition. In the near-IR, there are two components, a reprocessing component that also decreases (but not as much as in the optical) during the transition, however, the synchrotron does not, which results in the removal of the blue spectral component during the dips (see Fig. 6). If the accretion proceeds through the occasional penetration of the clumps/blobs of plasma through the magnetic barrier, the following scenario can lead to the observed near-IR/optical CCF. Consider the hot accretion flow with the inner radius close to the magnetospheric radius and emitting through the synchrotron self-Compton mechanism (similar to the hot flows in black hole X-ray binaries; Poutanen & Veledina 2014). If there is a local increase in the mass transfer rate, then the accretion flow becomes inhomogeneous and the resulting spectrum depends on the local number density of electrons. For a higher electron number density the (near-IR) synchrotron emission is suppressed due to the increased self-absorption. The inhomogeneities in the hot accretion flow containing a higher electron number density have a higher chance to penetrate through the magnetic barrier, hence once there is a sufficiently dense plasmoid, with the near-IR synchrotron emission suppressed, the flow accretes/drifts towards the compact object causing an increase in the X-ray emission. The X-ray emission triggers the reprocessing in the disc, both in the optical and near-IR (likely without a significant delay between them). The plasmoids are then expelled by the rotating magnetic field, forming an outflow and giving rise to the increase of the synchrotron near-IR emission as the plasmoids become optically thin. At the same time, the X-ray luminosity drops and the source switches to the passive state. Indeed, these ideas are further supported by the fact that transition from the X-ray active to X-ray passive state is always accompanied by a radio brightening, which has been interpreted as being due to rapid ejections synchrotron-emitting plasma by the pulsar (Bogdanov et al. 2018).

The near-IR/optical CCF can be explained by two components: synchrotron emission from plasmoids and reprocessing. The dip at negative lags corresponds to the suppression of the near-IR synchrotron emission of the plasmoids in hot accretion flow, which occurs just before the X-ray switches to the active state. The narrow peak at ~5 s corresponds to the delayed reprocessed component, enhanced by the increased X-ray emission (O'Brien et al. 2002). The broad positive correlation at positive lags is driven by the increased synchrotron emission of the outflowing plasmoids, which become optically thin as they expand. The width of the anticorrelation and broad positive correlation corresponds to the characteristic time-scale for the penetration of the (entire) inhomogeneity into the magnetosphere, which is roughly comparable to the viscous time-scale at the magnetospheric radius. In the r'-band light curves, this corresponds to the average duration of the active state.

In Fig. 10 we show model predictions for the optical and near-IR ACFs and CCFs expected from the hot accretion flow model. Our aim is to show that the model can indeed reproduce the main features of the CCFs. We leave the detailed modelling to a future paper, as it involves a number of unknown parameters for the disc and synchrotron components. To model the ACFs and CCFs, we simulate the light curve as mass accretion rate fluctuations from a prescribed PDS shape using the Timmer & Koenig (1995) algorithm. We assume that the X-ray light curve is proportional to the mass accretion rate light curve. We assume a zero-peak Lorentzian profile for the PDS accretion rate and equal contributions of the disc and synchrotron components. The disc to synchrotron ratio determines the relative importance of the dip and peak in the CCF (Veledina et al. 2017). The r'-band light curve is obtained by convolving the X-ray light curve with the accretion disc transfer function. The synchrotron emission of the plasmoids is simulated through the mean-subtracted accretion rate light curve. For the radiation of the hot flow we take this light curve with a minus sign (similar to equation 2 of Veledina et al. 2011) and shift it in time so that it leads the X-rays. The synchrotron emission of expanding plasmoids is modelled as the accretion rate light curve, shifted in time towards positive lags, i.e. it comes after the X-rays. The K_s band contains the synchrotron components of the plasmoids and the reprocessed component. The main parameters affecting the shape of the CCF are the assumed PDS shape of the mass accretion rate fluctuations and relative contribution of various synchrotron/disc components. The model predictions for the optical and near-IR ACFs and CCFs expected are shown in Fig. 10. As one can see there is a remarkable agreement in the general features predicted by the model with what is observed, a broad negative anticorrelation at negative lags, a broad positive correlation at positive lags, with a strong, positive narrow correlation superimposed.

If the active-state luminosity $L_X \sim 3 \times 10^{33}$ erg s^{-1} (Archibald et al. 2015; Bogdanov 2015) is due to accretion, i.e. $L = G M \dot{M}/R$, where the neutron star mass is $M = 1.71\,M_\odot$ (Deller et al. 2012), radius $R = 12$ km (Nättilä et al. 2016), and G is the gravitational constant, then the accretion rate is $\dot{M} = 1.5 \times 10^{13}$ g s^{-1}. With this mass inflow rate at the magnetospheric boundary, the active-state magnetospheric radius (the radius when the pressure of the neutron star magnetosphere is able to halt the inflowing matter) is $R_m \sim 150$ km, assuming a dipole magnetic field with strength $B \sim 10^8$ G (Archibald et al. 2009; Deller et al. 2012). In the passive state, the mass inflow rate is likely smaller, leading to a higher magnetospheric radius. The corotation radius (at which the matter in Keplerian orbit corotates with the neutron star) is $R_{co} = 24$ km and the light cylinder radius (at which field lines anchored to the neutron star rotate at the speed of light) is $R_{lc} = 80$ km. Hence for such low X-ray luminosities, the magnetospheric radius exceeds the light cylinder radius, and by far exceeds the corotation radius. This implies that the hot flow has to be truncated outside of the light cylinder, $\gtrsim 100$ km. The viscous time-scale at this radius is of the order of a few 100 s, which is roughly consistent with the width of the negative dip and broad peak in the CCF. The magnetic field inside the flow is likely self-generated by the flow and can be much lower than at the neutron star surface. We estimate the magnetic field inside the flow using condition that the turnover frequency is close to K_s band and the requirement for the observed synchrotron luminosity is equal to the synchrotron luminosity at the turnover frequency. Using equation (6) of Veledina et al. (2013) for the K_s-band flux at a radius of ~100 km and a distance of 1.368 kpc (Deller et al. 2012), we obtain a rough estimate for the magnetic field strength inside the hot flow of $B \sim 10^4$ G, which is comparable to the magnetic field of the pulsar at this radius. We leave the detailed spectral and timing modelling of the observed characteristics to a future paper.
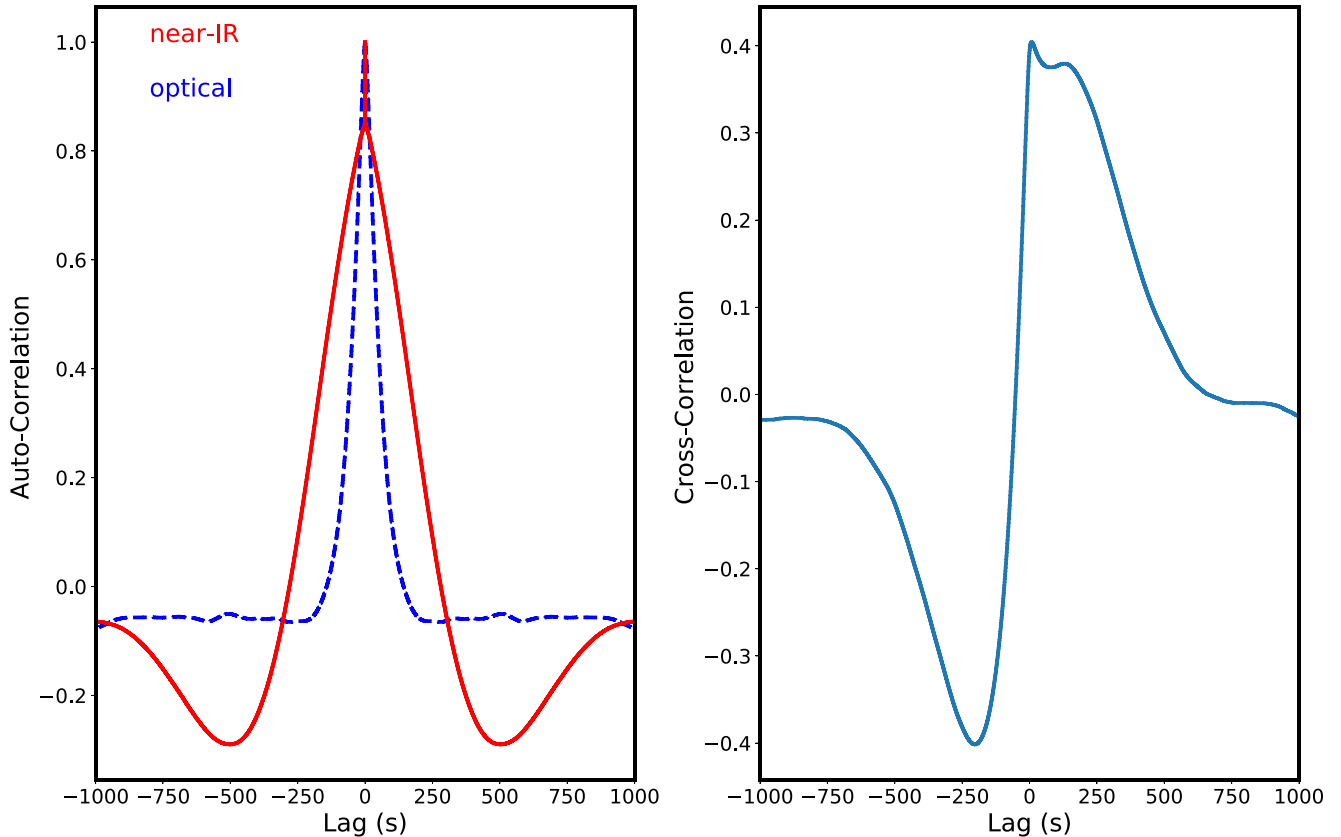
Figure 10. Model predictions for the optical and near-IR ACFs and CCF. Left: the optical (blue dashed line) and near-IR (red solid line) ACFs. Right: the optical and near-IR CCF. The model considers a hot accretion flow of Veledina et al. (2011) with the inner radius close to the magnetospheric radius of the neutron star. The near-IR/optical CCF can be explained by two components: synchrotron emission of plasmoids and reprocessing. The dip at negative lags corresponds to suppression of the near-IR synchrotron emission of the plasmoids in hot accretion flow. The narrow peak at ∼5 s corresponds to the delayed reprocessed component, enhanced by the increased X-ray emission. The broad positive correlation at positive lags is driven by the increased synchrotron emission of the outflowing plasmoids.

5 CONCLUSION

Below we list the main results of this paper.

(i) Our simultaneous r'- and K_s-band light curves show rectangular, flat-bottomed dips, similar to the X-ray mode-switching (active–passive state transitions) behaviour observed previously. During the active–passive state transition, the r'/K_s flux ratio decreases due to the larger decrease in the r'-band flux compared to the K_s-band flux. The SED of the dips (active minus passive flux) shows a turnover between the r'- and K_s band.

(ii) The CCF of the optical and near-IR data reveals a strong, broad negative anticorrelation and negative lags, a broad positive correlation at positive lags, with a strong, positive narrow correlation superimposed. The shape of the CCF resembles the optical/X-ray CCF observed in the black hole X-ray binary Swift J1753.5−0127, but the time-scales are different. The difference can be explained by the presence of a solid surface and the pulsar's magnetosphere in PSR J1023+0038.

The active–passive transition and features in the CCF can be explained by reprocessing and a hot accretion flow close to the neutron star's magnetospheric radius. Since the accretion disc is truncated at distance comparable to the magnetospheric radius, the characteristic viscous time-scales are longer than in black hole binaries, giving broader features in the CCF. The optical emission is dominated by the reprocessed component, whereas the near-IR emission

contains a component due to the emission from plasmoids in the hot accretion flow and a reprocessed component.

The rapid transitions between the active and passive states are due to the penetration of the hot accretion flow material on to the neutron star and the expelling of the blobs of synchrotron emitting plasma fed by the hot inner flow from the magnetosphere. The plasmoids are expelled by the rotating magnetic field of the neutron star, giving rise to the increase of the synchrotron near-IR emission as they expand and become optically thin. During the active–passive transition the optical reprocessing component decreases that results in the removal of a blue spectral component. The combination of the red synchrotron spectrum with the blue reprocessed spectrum also produces the observed SED. The dip at negative lags corresponds to the suppression of the near-IR synchrotron component in the hot flow, whereas the broad positive correlation at positive lags is driven by the increased synchrotron emission of the outflowing plasmoids. The narrow peak in the CCF is due to the delayed reprocessed component, enhanced by the increased X-ray emission. The accretion of clumpy material through the magnetic barrier of the neutron star produces the observed near-IR/optical CCF and variability.

REFERENCES

Alpar M. A., Cheng A. F., Ruderman M. A., Shaham J., 1982, Nature, 300, 728

Ambrosino F. et al., 2017, Nat. Astron., 1, 854

Archibald A. M. et al., 2009, Science, 324, 1411

Archibald A. M. et al., 2015, ApJ, 807, 62

Bassa C. G. et al., 2014, MNRAS, 441, 1825

Bogdanov S., Halpern J. P., 2015, ApJ, 803, L27

Bogdanov S., Patruno A., Archibald A. M., Bassa C., Hessels J. W. T., Janssen G. H., Stappers B. W., 2014, ApJ, 789, 40

Bogdanov S. et al., 2015, ApJ, 806, 148

Bogdanov S. et al., 2018, ApJ, 856, 54

Cardelli J. A., Clayton G. C., Mathis J. S., 1989, ApJ, 345, 245

Deller A. T. et al., 2012, ApJ, 756, L25

de Martino D. et al., 2013, A&A, 550, A89

Durant M., Gandhi P., Shahbaz T., Fabian A. P., Miller J., Dhillon V. S., Marsh T. R., 2008, ApJ, 682, L45

Durant M., Gandhi P., Shahbaz T., Peralta H. H., Dhillon V. S., 2009, MNRAS, 392, 309

Durant M. et al., 2011, MNRAS, 410, 2329

Edelson R. A., Krolik J. H., 1988, ApJ, 333, 646

Eikenberry S. S., Matthews K., Murphy T. W., Jr, Nelson R. W., Morgan E. H., Remillard R. A., Muno M., 1998, ApJ, 506, L31

Eikenberry S. S. et al., 2017, preprint (arXiv:1709.05542)

Fender R. P., Pooley G. G., Brocksopp C., Newell S. J., 1997, MNRAS, 290, L65

Gandhi P. et al., 2008, MNRAS, 390, L29

Gandhi P. et al., 2010, MNRAS, 407, 2166

Halpern J. P., Gaidos E., Sheffield A., Price-Whelan A. M., Bogdanov S., 2013, Astron. Telegram, 5514

Horne J. H., Baliunas S. L., 1986, ApJ, 302, 757

Hynes R. I., Charles P. A., Casares J., Haswell C. A., Zurita C., Shahbaz T., 2003, MNRAS, 340, 447

Kanbach G., Straubmeier C., Spruit H. C., Belloni T., 2001, Nature, 414, 180

Malzac J., Belloni T., Spruit H. C., Kanbach G., 2003, A&A, 407, 335

Malzac J., Merloni A., Fabian A. C., 2004, MNRAS, 351, 253

Nättilä J., Steiner A. W., Kajava J. J. E., Suleimanov V. F., Poutanen J., 2016, A&A, 591, A25

O'Brien K., Horne K., Hynes R. I., Chen W., Haswell C. A., Still M. D., 2002, MNRAS, 334, 426

O'Connor P., Golden A., Shearer A., 2005, ApJ, 631, 471

Pacini F., Salvati M., 1983, ApJ, 274, 369

Pahari M., Gandhi P., Charles P. A., Kotze M. M., Altamirano D., Misra R., 2017, MNRAS, 469, 193

Papadakis I. E., Lawrence A., 1993, MNRAS, 261, 612

Papitto A. et al., 2013, Nature, 501, 517

Papitto A., de Martino D., Belloni T. M., Burgay M., Pellizzoni A., Possenti A., Torres D. F., 2015, MNRAS, 449, L26

Parfrey K., Spitkovsky A., Beloborodov A. M., 2017, MNRAS, 469, 3656

Patruno A. et al., 2014, ApJ, 781, L3

Peterson B. M., 2001, in Aretxaga I., Kunth D., Mújica R., eds, Advanced Lectures on the Starburst–AGN Connection. World Scientific Press, Singapore, p. 3 doi:10.1142/9789812811318_0002

Poutanen J., Veledina A., 2014, Space Sci. Rev., 183, 61

Poutanen J., Veledina A., Revnivtsev M. G., 2014, MNRAS, 445, 3987

Press W. H., Teukolsky S. A., Vetterling W. T., Flannery B. P., 1992, Numerical Recipes in FORTRAN: The Art of Scientific Computing. Cambridge Univ. Press, Cambridge

Radhakrishnan V., Srinivasan G., 1982, Curr. Sci., 51, 1096

Robertson D. R. S., Gallo L. C., Zoghbi A., Fabian A. C., 2015, MNRAS, 453, 3455

Shahbaz T., Dhillon V. S., Marsh T. R., Zurita C., Haswell C. A., Charles P. A., Hynes R. I., Casares J., 2003, MNRAS, 346, 1116

Shahbaz T., Hynes R. I., Charles P. A., Zurita C., Casares J., Haswell C. A., Araujo-Betancor S., Powell C., 2004, MNRAS, 354, 31

Shahbaz T., Dhillon V. S., Marsh T. R., Casares J., Zurita C., Charles P. A., Haswell C. A., Hynes R. I., 2005, MNRAS, 362, 975

Shahbaz T., Dhillon V. S., Marsh T. R., Casares J., Zurita C., Charles P. A., 2010, MNRAS, 403, 2167

Shahbaz T., Russell D. M., Zurita C., Casares J., Corral-Santana J. M., Dhillon V. S., Marsh T. R., 2013, MNRAS, 434, 2696

Shahbaz T. et al., 2015, MNRAS, 453, 3461

Stappers B. W. et al., 2013, Astron. Telegram, 5513

Stappers B. W. et al., 2014, ApJ, 790, 39

Takata J. et al., 2014, ApJ, 785, 131

Tendulkar S. P. et al., 2014, ApJ, 791, 77

Timmer J., Koenig M., 1995, A&A, 300, 707

Veledina A., Poutanen J., Vurm I., 2011, ApJ, 737, L17

Veledina A., Poutanen J., Vurm I., 2013, MNRAS, 430, 3196

Veledina A., Revnivtsev M. G., Durant M., Gandhi P., Poutanen J., 2015, MNRAS, 454, 2855

Veledina A., Gandhi P., Hynes R., Kajava J. J. E., Tsygankov S. S., Revnivtsev M. G., Durant M., Poutanen J., 2017, MNRAS, 470, 48

Zurita C., Casares J., Shahbaz T., 2003, ApJ, 582, 369

This paper has been typeset from a TeX/LaTeX file prepared by the author.